High fidelity analysis to predict failure in T-joints

Zsombor Sápi[a*], Richard Butler[a], Andrew Rhead[a]

[a] Materials and Structures Research Centre, Department of Mechanical Engineering, University of Bath, Claverton Down, Bath, BA2 7AY, United Kingdom

Abstract

Composite T-joints and similar skin-stiffener joints have a central role in aerospace structures. However, their accurate numerical analysis is still a great challenge due to their complex geometry and stress state during loading. In this work, an experimentally validated high-fidelity finite element model is developed to simulate the failure of a T-joint subjected to tensile loading. For the first time in literature, the model accounts for the shape of the manufactured filler, ply thickness variability in the laminate, stress gradient across the ply thickness, thermal stresses and in-situ mechanical properties. A new phenomenon called "filler effective ply thickness" is introduced to address the increased strength of the filler when embodied in a laminate. With this method, the model predicted the location and the failure initiation load within 5% accuracy of the experimental specimens, whereas conventional approaches using unidirectional strength significantly underpredicted the strength of the joint.

Keywords

Noodle, Filler, Stiffener, LaRC05, In-situ strength

[*] Corresponding author. E-mail address: Z.Sapi@bath.ac.uk

1. Introduction

Due to their high specific strength and stiffness compared to their aluminium counterparts, composite and aluminium-composite skin-stiffener joints [1,2] are becoming widely used in aerospace structures. However, manufacturing constraints, such as the minimum radius a ply can be bent to, require the formation of a deltoid zone in the junction of the skin, flanges and web. This void is usually filled with a rolled unidirectional (UD) ply filler, also known as a "noodle".

Because of the complexity of the geometry and the stress state around the filler, there is no accurate analytical failure prediction method available. Therefore, a great deal of research has been focused on the numerical failure prediction of fillers [3]. Hélénon et al. investigated T-joints subjected to tensile loading [4]. The finite element model used cohesive elements and no specific ply failure criterion was implemented, and it overpredicted the strength of the joint by 225%. Only by directly modelling the crack propagation path with through-the-thickness cohesive elements based on the experimental results could the model predict the initial failure load with 25% accuracy. A predefined crack path was required in the FEA model in a similar investigation by Chen et al. where the crack initiated in the filler [5]. Bai et al. [6] used a progressive damage model based on the Hashin failure criterion and cohesive model to detect the initial failure of a π-joint under tensile loading. The numerical model underpredicted the initial failure load by 21%. However, the ultimate failure load was matched with 5% accuracy. Zhao et al. developed several models to predict the failure of π-joints based on Tsai-Wu, Hashin, Modified Hashin and Maximum Stress criteria. The initial failure loads were captured within 2-20% accuracy depending on the criteria used, but the reported images of manufactured test samples show severe wrinkling in the skin and a deformed noodle shape [7,8]. A numerical model with extensive use of cohesive elements was proposed by Cui to

predict the failure behaviour of a T-joint, but it utilised a foaming rubber instead of a CFRP noodle [9].

There are several approaches available in the literature intended to capture the failure of out-of-plane joints. However, in many cases, the manufacturing quality is not sufficient for numerical modelling, or the finite element model lacks the capability of capturing the undergoing failure mechanisms. This paper first introduces a method to manufacture a T-joint with high-quality filler, adequate laminate consolidation and post-manufacturing procedures to ensure repeatability, which are required for accurate numerical modelling. Then, a highly flexible parametric finite element model is presented that, for the first time in literature, can account for the unique shape of the filler, the variability of the ply thickness across the joint and the in-situ behaviour of the filler via its effective ply thickness. As the failure of out-of-plane joints is usually unstable and results in a sudden drop in the stiffness of the joint, which drives the design of the component, the framework presented here aims to capture the initiation of the failure. The failure of the T-joint subjected to tensile (pull-off) loading is then evaluated by the LaRC05 failure criterion and cohesive surfaces. Finally, comparative studies are carried out to demonstrate the importance of thermal expansion, in-situ strengths and mesh refinement.

2. Experimental setup

2.1 Manufacturing

Six specimens denoted as A1-A6 were tested under pull-off (tensile) loading with the geometry and boundary conditions shown in Fig. 1. Hexcel HexPly® AS4/8552 unidirectional prepreg material was used with a nominal cured ply thickness (CPT) of 0.196 mm. The layup was symmetric and balanced independently in the overlaminate and skin with stacking sequences of $[90/45/0/-45]_{2s}$ and $[90/45/0/-45]_{3s}$, respectively, where 0° is aligned in the Z direction. The

symmetricity is not present in the flanges where the two layups join, but the thicker skin was required to alleviate the spring-back of the flanges after cool down. The plies in the overlaminate are referred to as Ply 1 to Ply 16, with Ply 1 being adjacent to the filler.

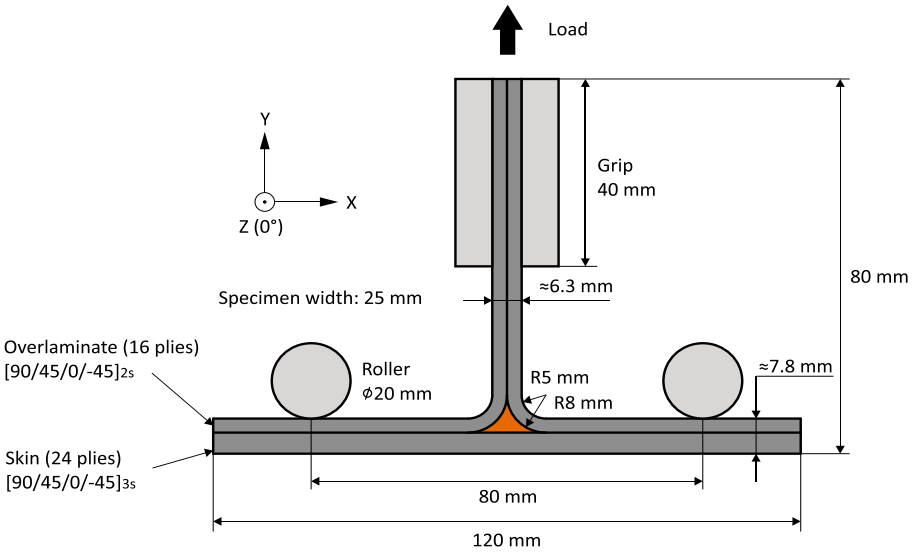

Fig. 1. Specimen geometry and test setup

The filler was manufactured by manually rolling the same unidirectional material with fibres oriented along the Z-axis. Then, the noodle was placed into a noodle forming tool (Fig. 2a) with 8 mm radius, and the final geometry was achieved by a two-step procedure. First, heat was applied with a heat gun to increase formability while the filler was preformed with a caul plate and manual pressure, then the tool was closed and vacuum bagged to undergo a debulking stage under >95% vacuum for 15 minutes. The correct amount of material in the filler and the geometry of the noodle forming tool have utmost importance in order to avoid an under or oversized noodle, which can result in skin wrinkling and reduced joint strength [10]. With 5 mm radius on the outside surface of the joint (Fig. 1) and the aforementioned CPT of the material in the overlaminate, the theoretical radius of the filler should be 8.14 mm. Taking into consideration the standard sizes of radius cutter end mills and the expected CPT reduction in the radius of the overlaminate, the noodle forming tool used in this study was manufactured

with R = 8 mm radius. The required amount of material for the filler (V) was calculated according to the following equation:

$$V = R^2\left(2 - \frac{\pi}{2}\right) \tag{1}$$

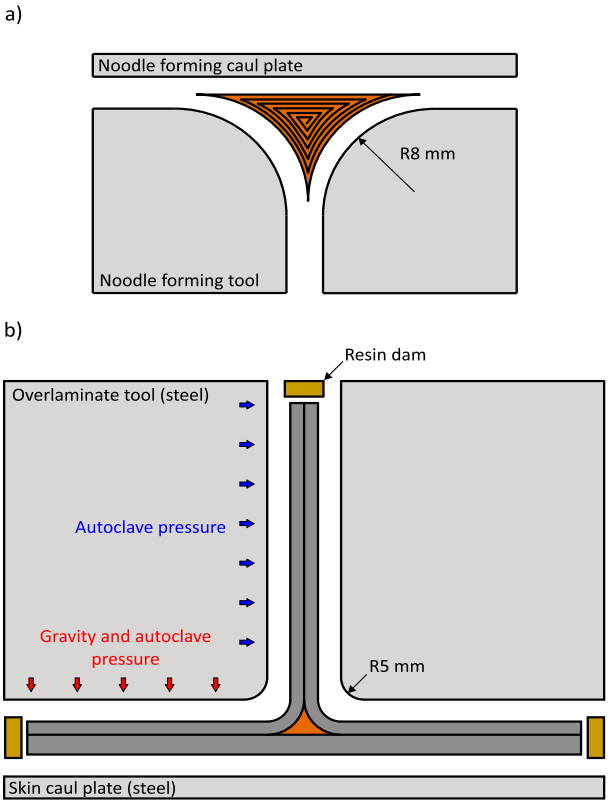

Fig. 2. a) Noodle forming tool b) T-joint tool

A floating tool setup was utilised with two overlaminate tools and a caul plate for the skin (Fig. 2b). After laying up 4 plies of each subassembly, the tools were vacuum bagged and debulked to remove air bubbles trapped between the layers. After the final assembly, the openings were sealed with resin dams to maintain the resin content and CPT of the material while enabling the tool surfaces to apply pressure on the plies. Instead of using a closed tool, the floating tool eliminated possible manufacturing defects and poor consolidation of the laminate as a result of over-thick layup or tool stand-off [11]. The tools were made of steel, which has a lower coefficient of thermal expansion than aluminium and higher bending stiffness than an

equivalent L-shaped composite tool. To ensure the consistent temperature distribution of the tools during curing, the lowest allowed heat and cool down rates were chosen according to the manufacturer's datasheet [12]: heat at 1 °C/min up to 110 °C, hold for 1 hour, heat at 1 °C/min up to 180 °C, hold for 2 hours, cool at 2 °C/min to room temperature.

After removing the T-joint from the tool and cutting it to individual samples with a diamond plated saw, the surfaces were ground up to P2500 quality (8 µm size) with Buehler Apex Diamond Grinding Discs (DGD). The surface roughness was evaluated by a Proscan 2000 profilometer equipped with a chromatic sensor capable of measurement down to 5 nm accuracy: ISO R_a = 0.461 µm, R_z = 2.866 µm, R_{max} = 4.528 µm. The dimensions of the specimens were measured with a micrometre and the CPT and filler area were measured using micrographs and CorelDRAW.

2.2 Testing

The specimens were heated up to 120 °C for 2 hours prior testing to eliminate the moisture content accumulated after manufacturing. The tensile tests were carried out at 2 mm/min crosshead displacement rate and at room temperature with an Instron 3369 machine and 50 kN load cell. Both sides of the specimens were recorded with Phantom VEO 410L high-speed cameras and displacement was taken as the crosshead displacement of the Instron machine.

3. Numerical model

3.1 Geometry

The importance of accurate filler and joint geometry has been demonstrated in many cases in the literature [3]. For this reason, a high-fidelity implicit Abaqus FEA model was developed in which the geometry can be fine-tuned and matched with the actual specimen geometry based on micrograph images and measurements. The model is based on a parametric Python script,

and its capabilities are shown in Fig. 3. The most critical features are the independent ply thicknesses in the flanges, web and radius, and the cross-sectional area and shape of the filler, where the latter is achieved by separately specifying the filler edge positions and the curvature of the radius. This was implemented in order to account for the difference in manufactured filler shape compared to the idealised value owing to the resin flow during curing, which results in a unique consolidation behaviour described in section 4.1. The method used to define the curvature can break the continuity of surfaces that defined the overlaminate thickness when significantly different CPT values are used in the overlaminate. However, small levels of discontinuity are acceptable and indeed necessary to eliminate the geometrical singularity of the filler edges. A similar approach was used in the literature [4].

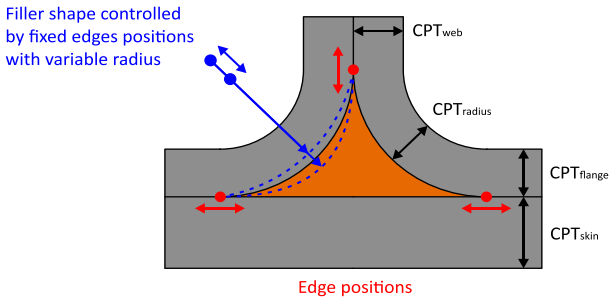

Fig. 3. Variable parameters of the FEA model around the filler to match the actual specimen geometry

3.2 Boundary conditions

A 3D slice model having 0.1 mm width along Z-axis and plane strain conditions applied on both faces was used for the analysis. The width was selected to ensure adequate element aspect ratio in the filler region of the joint and the results taken from the simulation were scaled up to the nominal 25 mm afterwards. The 3D slice method was shown to be a sufficient way to model the failure of similar structures [4,13]. Moreover, a 3D model would not only require higher computational times because of increased element number across the width of the

specimen (Z-axis), but also further mesh refinement to account for the stress concentrations due to the free-edge effect on the faces and their contribution to the failure model.

The simulation consisted of a thermal and a mechanical step. During the first, the geometry could deform freely in the X-Y-plane and the cool down was simulated with a drop from 180 °C cure temperature to 25 °C room temperature. This was followed by the mechanical step, where the roller constraints were applied as zero displacements along Y-axis of the relevant nodes and the loading was applied as displacement on the top surface of the specimen.

3.3 Meshing

C3D8 brick elements were used in every part of the model except for the filler, which required C3D6 wedge elements too to accommodate for its sharp edges. Higher order C3D20 and C3D15 elements did not produce significant difference and therefore the desired fidelity was achieved by increasing the mesh density rather than by increasing the polynomial order of an element.

Mesh sensitivity studies were carried out in different areas. The first step was to allocate a double biased mesh on the side and bottom surfaces of the filler so that the mesh became refined approaching the edges. This pattern was matched in the radius in the overlaminate. The mesh inside the filler did not need refinement as the failure only initiated on its surfaces based on simulation and experimental results. Outside these zones, the web and flanges used a coarse mesh, as failure, large deformations and stress concentrations did not occur in these areas.

The number of elements across ply thickness had a great impact on the accuracy of the model. The most significant difference occurred between 1 and 2 through-thickness elements; using the latter it is possible to predict on which side of the ply the failure initiates, which influences the behaviour of the cohesive surfaces placed between each ply. Further increasing the

number of elements increased the accuracy up to 4 elements. Above this, the increased computational requirement did not justify the marginal increase in accuracy. The effect of the number of elements across ply thickness along with the overview of the mesh used around the filler is shown in Fig. 4. The maximum and average of the nodal stress values of the elements converged by using 2 elements, but the minimum values only converged below 5% difference after increasing the number of elements to 4.

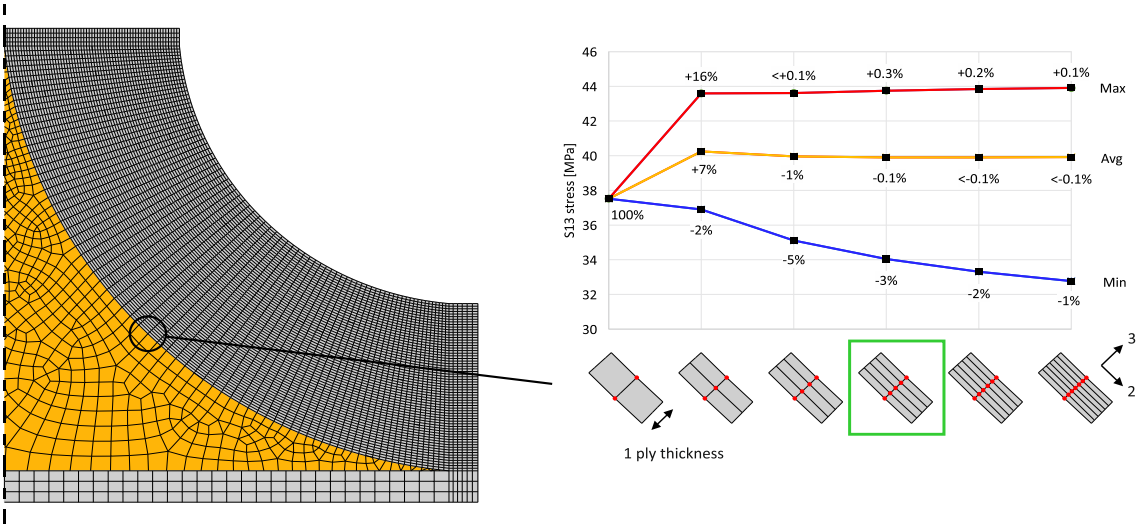

Fig. 4. Final mesh around the filler and the mesh convergence study. The selected mesh density (4 elements across ply thickness) is highlighted with green

3.4 Failure criterion and material properties

The FEA model in this study could predict matrix, fibre tensile, fibre kinking and fibre splitting failure initiation according to the LaRC05 failure criterion, which was implemented as a user material subroutine (UMAT). The most relevant features of the criterion are described below, whereas the detailed explanation of the underlying theory is described in [14]. Delamination between the skin, the overlaminate and the filler and within the web and the flanges was detected by using cohesive surfaces between the plies.

3.4.1 LaRC05 failure criterion

The LaRC05 failure criterion predicts matrix failure according to Eq. (2).

$$FI_M = \left(\frac{\tau_T}{S_T^{is} - \eta_T \sigma_N}\right)^2 + \left(\frac{\tau_L}{S_L^{is} - \eta_L \sigma_N}\right)^2 + \left(\frac{\langle \sigma_N \rangle_+}{Y_T^{is}}\right)^2 \quad (2)$$

The terms τ_T, τ_L and σ_N are the traction components of the matrix fracture plane (Fig. 5) and are obtained according to Eqs. (3-5). α is the angle which maximizes FI_M and is numerically obtained by evaluating the equations for $0° \leq \alpha < 180°$.

$$\tau_T = \frac{\sigma_2 + \sigma_3}{2} + \frac{\sigma_2 - \sigma_3}{2}\cos(2\alpha) + \tau_{23}\sin(2\alpha) \quad (3)$$

$$\tau_L = -\frac{\sigma_2 - \sigma_3}{2}\sin(2\alpha) + \tau_{23}\cos(2\alpha) \quad (4)$$

$$\sigma_N = \tau_{12}\cos(\alpha) + \tau_{31}\sin(\alpha) \quad (5)$$

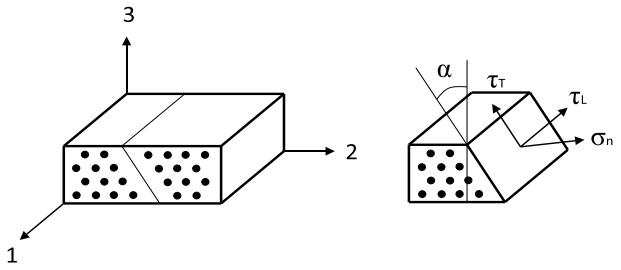

Fig. 5. Matrix fracture plane and traction components

Transverse and longitudinal friction coefficients η_T and η_L are calculated according to Eq. (6-7) and α_0 refers to the matrix fracture angle used as 53° in this study according to [15]. S_L^{UD} and Y_C^{UD} are unidirectional longitudinal shear strength and transverse compressive strength, respectively.

$$\eta_T = -\frac{1}{\tan(2\alpha_0)} \quad (6)$$

$$\eta_L = -\frac{S_L^{\mathrm{UD}}\cos(2\alpha_0)}{Y_C^{UD}\cos^2(\alpha_0)} \quad (7)$$

The calculation and implementation of in-situ strengths (S_T^{is}, S_L^{is} and Y_T^{is}) are described in section 3.4.2.

Fibre kinking and splitting are evaluated by Eq. (8), depending on the value of longitudinal compressive stress: $\sigma_1 \leq -X_C/2$ indicates fibre kinking and $\sigma_1 \geq -X_C/2$ indicates fibre splitting, where X_C is the longitudinal compressive strength of the material.

$$FI_{KINK} = FI_{SPLIT} = \left(\frac{\tau_{23}^m}{S_T^{is} - \eta_T \sigma_2^m}\right)^2 + \left(\frac{\tau_{12}^m}{S_L^{is} - \eta_L \sigma_2^m}\right)^2 + \left(\frac{\langle \sigma_2^m \rangle_+}{Y_T^{is}}\right)^2 \quad (8)$$

The terms denoted with m superscript refer to the stresses in the misalignment plane. However, under this specific loading condition, the T-joints did not sustain significant compressive stresses at any time during the simulation, thus these failure modes are not discussed in this work. For the detailed theory behind the calculation of these failure indices, the authors refer to [14].

Fibre tensile failure is evaluated by Eq. (9), where X_T is the longitudinal tensile strength of the material.

$$FI_{FT} = \frac{\langle \sigma_1 \rangle_+}{X_T} \quad (9)$$

3.4.2 In-situ strength

Compared to the ply strength measured with unidirectional specimens, in-situ strength refers to the increased transverse tensile, transverse compressive, in-plane and out-of-plane shear strengths of the ply as a result of the constraints set by the adjacent plies with different orientation. Moreover, it also depends on the location and thickness of the ply and the number of plies with same orientation stacked together.

The in-situ strengths were calculated according to [16–18]. The shear response factor (β), accounting for the non-linear shear behaviour of the material, was calculated by fitting a curve (Eq. 10) to the shear stress-strain curve of AS4/8552 published in [19].

$$\gamma_{12} = \frac{1}{G_{12}}\sigma_{12} + \beta\sigma_{12}^3 \tag{10}$$

In-situ strengths were applied for the T-joint presented in this paper according to the following principles (Fig. 6a):

- Thin outer ply strengths ($Y_T^{is,thin,o}$, $S_L^{is,thin,o}$, $S_T^{is,thin,o}$) were used for the outer plies in the laminate
- Thin embedded ply strengths with double ply thickness ($Y_T^{is,thin,e2}$, $S_L^{is,thin,e2}$, $S_T^{is,thin,e2}$) were used for the -45°/-45° plies within the overlaminate and skin and for the 90°/90° on the boundary of the overlaminate and skin
- Thin embedded ply strengths ($Y_T^{is,thin,e}$, $S_L^{is,thin,e}$, $S_T^{is,thin,e}$) were used for the rest of the plies in the laminate
- Thick ply strengths ($Y_T^{is,thick}$, $S_L^{is,thick}$, $S_T^{is,thick}$) were used for the filler.

The in-situ strength can be applied for the filler because the 0° fibres in it are constrained by the adjacent 90° ply on its surface. Its effective ply thickness (demonstrated in Fig. 6b) is larger than 0.8 mm, therefore the thick ply model was used [20]. It is notable that, approaching the edges of the filler, its effective ply thickness approaches zero, and thus the in-situ strength should vary accordingly. However, these locations in the filler are not subjected to high stresses in this particular T-joint configuration (see Fig. 9 and section 4.3) and therefore a variable in-situ strength model was not implemented.

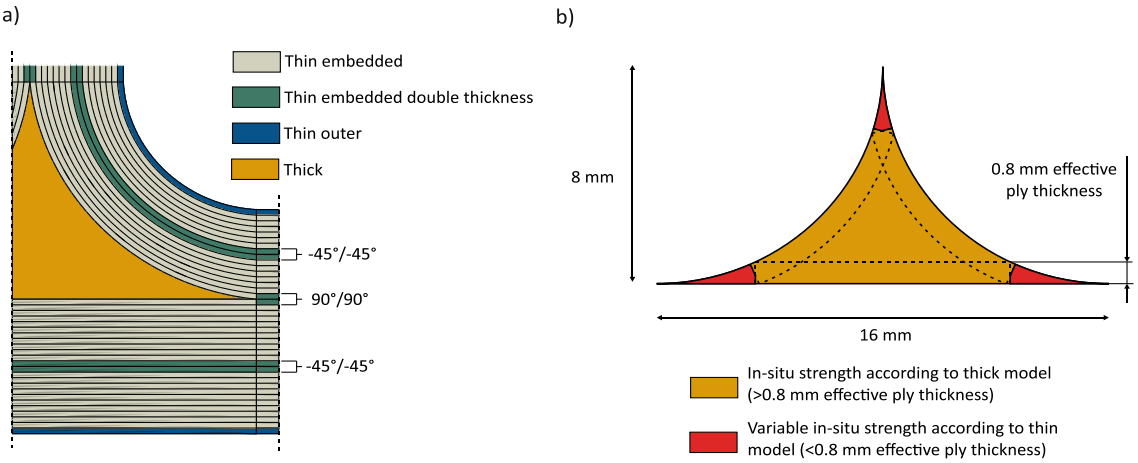

Fig. 6. a) In-situ strengths used in the FEA model b) Effective ply thickness of the filler. In this work, the whole filler was modelled with in-situ strength based on the thick model.

3.4.3 Cohesive surface

Delamination initiation was detected by using cohesive surfaces between every ply of the overlaminate, between the overlaminate and the skin and under the filler. As no failure occurred in the skin based on experimental results (see Fig. 8), the cohesive model was not utilised in this region to increase computational efficiency.

Damage initiation was based on the quadratic nominal stress criterion. The interface penalty stiffnesses (K_N, K_S, K_T) were calculated according to [21]. There are many approaches in literature about what stiffness values should be used for cohesive models, ranging from 10^5 MPa/mm [22] to 10^6 MPa/mm [23] magnitude, but results were not sensitive to this parameter in this work. One magnitude lower value than the used ones in Table 2 resulted in less than 5% change in cohesive failure indices. Interface strengths (σ_N^{int}, σ_S^{int}, σ_T^{int}) were taken as UD transverse tensile and shear strengths (Y_T^{UD}, S_L^{UD}).

The complete list of material properties used for the calculations and in the model can be found in Table 1-2. The S_T^{is}, S_L^{is} and Y_T^{is} in-situ strengths used in Eq. (2) are replaced by the

corresponding thin embedded, thin embedded with double ply thickness, thin outer and thick values depending on the location of the ply where the criterion is being calculated.

Table 1. Material properties used in the simulation

Property	Reference	Value
Ply elastic properties:		
E_1	[24]	137000 MPa
$E_2 = E_3$	[24]	8800 MPa
$G_{12} = G_{13}$	[24]	4900 MPa
G_{23}	[24]	2959 MPa
$\nu_{12} = \nu_{13}$	[24]	0.314
$\nu_{23} = \nu_{32}$	[24]	0.487
$\nu_{21} = \nu_{31}$	[24]	0.020
Ply strength properties:		
X_T	[24]	2106 MPa
X_C	[24]	1675 MPa
Y_T^{UD}	[24]	74.2 MPa
Y_C^{UD}	[24]	322 MPa
S_L^{UD}	[24]	110.4 MPa
Coefficients of thermal expansion:		
α_1	[24]	2.1x10^{-7}/°C
$\alpha_2 = \alpha_3$	[24]	3.3x10^{-5}/°C
Cohesive interface properties:		
σ_N^{int}	[24]	74.2 MPa
$\sigma_S^{int} = \sigma_T^{int}$	[24]	110.4 MPa
Fracture toughnesses:		
G_{IC}	[24]	0.30 kJ/m^2
G_{IIC}	[24]	0.87 kJ/m^2
Matrix fracture angle in uniaxial compression:		
α_0	[14]	53°

Table 2. Derived material properties used in the simulation. The values are calculated based on the referenced sources.

Property	Reference	Value
In-situ strengths:		
$Y_T^{is,thin,e}$	[18]	131.0 MPa
$Y_T^{is,thin,e2}$	[18]	92.6 MPa
$Y_T^{is,thin,o}$	[18]	82.9 MPa
$Y_T^{is,thick}$	[18]	117.5 MPa
$S_L^{is,thin,e}$	[18]	126.4 MPa
$S_L^{is,thin,e2}$	[18]	102.7 MPa
$S_L^{is,thin,o}$	[18]	102.7 MPa
$S_L^{is,thick}$	[18]	135.4 MPa
$S_T^{is,thin,e}$	[17]	138.9 MPa
$S_T^{is,thin,e2}$	[17]	112.8 MPa
$S_T^{is,thin,o}$	[17]	112.8 MPa
$S_T^{is,thick}$	[17]	148.8 MPa
Cohesive interface properties:		
K_N	[21]	2244898 MPa/mm
K_S	[21]	1250000 MPa/mm
K_T	[21]	754841 MPa/mm
β	[16,19]	2.1x10^{-8} MPa^{-3}
Coefficients of friction:		
η_T	[25]	0.287
η_L	[15]	0.261

4. Results and discussion

4.1 Manufactured specimen quality

A manufactured filler can be seen in Fig. 7. The specimens have 0.2 mm spring-back at the end of flanges in Y direction (in accordance with numerical results), there is no skin wrinkling present and the sizes of the resin-rich zones at the edges of the filler are insignificantly small. However, during the consolidation of the T-joint, the resin content reduces in the radius due to the geometry and the pressure set by the tool [26]. This leads to lower ply thickness in the radius (CPT_{radius} = 0.181 mm) compared to the flanges (CPT_{flange} = 0.187 mm; -3.2%), the web (CPT_{web} = 0.197 mm; -8.1%) and the nominal CPT ($CPT_{nominal}$ = 0.196 mm; -7.7%) averaged over the 6 specimens.

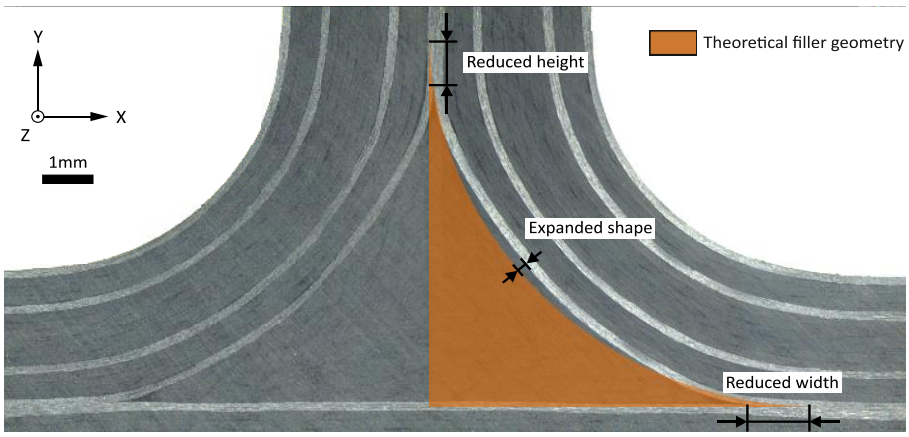

Fig. 7. Manufactured filler

By measuring the width and height of the noodle it was found that the height reduced from the theoretical 8 mm to an average of 6.8 mm and the width from the theoretical 16 mm to 13.4 mm. This resulted in a 3.6% reduction from the theoretical cross-sectional area of 27.5 mm^2 to average of 26.5 mm^2. In this case, the amount of cross-sectional area loss is insignificant and can be ignored, but in other applications, especially with incorrect tool setup, it might yield a higher value, producing a loss of resin content in the filler and reduced resin-

dominated material properties (such as transverse tensile strength) too. As for the shape of the filler, the reduction of the width and height was compensated by the expansion phenomenon of the noodle, leading to an analytically incorrect curvature (Fig. 7). In other words, the curvature of the noodle is not identical to the curvature of the outside of the overlaminate set by the tool geometry (R = 5 mm). Hence, there is a variation in ply thickness between the web, radius and flange.

The ply thickness variability and noodle shape were accounted for in the FEA model as described in section 3.1.

4.2 Failure mechanisms

The load-displacement curves of the experimental tests and finite element analysis can be seen in Fig. 8 and the values of failure loads in Table 3. The typical failure mechanism is also shown in Fig. 8.The slacks during the application of the load in the actual experimental curves were eliminated by extending the linear stage of the graphs to the X-axis using the joint stiffness during the load-up stage. The simulation was stopped at the first event of an element reaching the failure index value 1 for any criterion.

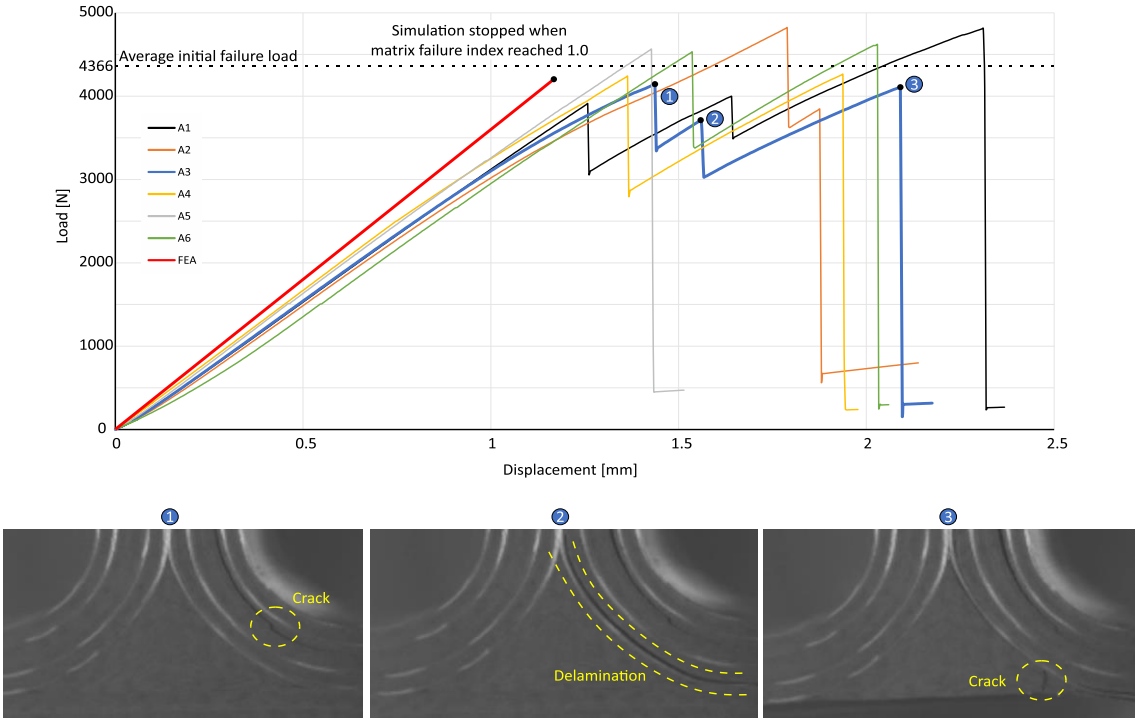

Fig. 8. Load-displacement curves of the experimental tests and simulation with typical failure mechanisms shown on A3 specimen

Table 3. Experimental and numerical test results

Specimen ID	**Initial failure load [N]**	**Ultimate failure load [N]**
A1	3907	4811
A2	4818	-
A3	4147	-
A4	4235	4257
A5	4560	-
A6	4527	4617
Average	4366	4562
SD	330	281
FEA	4229	-
Difference	-3.1%	-

The difference between the stiffness prediction of the FEA model and the experimental results can be accounted for the difference in material properties. The skin, which has a higher thickness than the overlaminate, undergoes compression during the application of the mechanical loading, but the use of compressive elastic modulus of the material is not implemented in the model and the tensile value is used instead. The compressive elastic

modulus of the AS4/8552 material in fibre direction is 17% lower than its tensile elastic modulus [24].

The failure initiation was identical in five of the six specimens (A1, A2, A3, A4 and A6). After the linear load-up stage a crack initiated on the outer surface of the -45°/-45° stack (Plies 8 and 9) in the radius. This crack immediately jumped through the 0° ply (Ply 10) and developed into delaminations between the -45°/-45° stack and 0° ply, and between the 0° ply and 90° ply (Ply 11) propagating downwards and upwards along the radius. The subsequent load drop was in the range of 800-1400 N.

In specimens A1, A2 and A3 this was shortly followed by an additional delamination in the radius corresponding to the second load drop in their curves. Specimen A1 failed between the -45° and 90° interface (Plies 4 and 5), A2 failed between the 90° and 45° interface (Plies 5 and 6), whereas A3 failed on the boundary of the filler and the first 90° ply.

With the exception of specimen A5, the joints withstood further loading, which in some cases resulted in a larger ultimate failure load than the initial values. The last failure event was the vertical cracking of the filler. This occurred in the lower region of the filler surface and propagated down to the skin. The upper end of this crack triggered delamination between the filler and the 90° ply spreading up to the web, whereas the bottom end caused the delamination of the skin from the filler and overlaminate.

In specimen A5, the laminate in the radius did not fail first, instead, the filler cracked in the same way as described above and caused sudden failure of the joint.

After failure initiation, neither of the joints demonstrated pseudo-ductile behaviour and their load-bearing capability dropped by an average of 36%. The loss of structural integrity on the first appearance of damage eliminates the applicability of design for ultimate failure practice

and shows that prediction of the initial failure of the component is the driving factor for design.

4.3 Numerical results

The lowest compressive stress occurring in the model is addressed in section 4.4.1, but it was too low to trigger failure according to the fibre compressive (kinking and splitting) criteria. Hence, shear and tensile stresses are critical for the failure of the joint and only the matrix and fibre tensile criteria are discussed here.

The onset of failure initiation took place at 4229 N applied load when the LaRC05 matrix failure index reached the value of 1 (Fig. 9a). This load is 3.1% lower than the average initial failure load of the experimental tests. The location of the element is highlighted and it is in accordance with the location of the crack from the experimental results in Fig. 8 (see Fig. 10 for direct comparison). The element failed at α = 38° matrix fracture plane angle, and the values of traction components (τ_T, τ_L, σ_N, see Eq. 3-5), which are evaluated against the in-situ ply strengths in the criterion, are shown in Fig. 9b-d. The dominant stress is the σ_N = 88.5 MPa normal component (Fig. 9d), which is responsible for 92% of the 1.0 failure index value (third part of Eq. 2). This stress state supports the underlying phenomenon as the applied tensile load tries to "open up" the radius and straighten the curvature of the ply along Y-axis. From the aspect of in-situ strengths, Plies 8 and 9 (-45°/-45° stack) behave as one embedded ply with double ply thickness, hence the in-situ transverse tensile strength is lower compared to the one of a single embedded ply (from 131 MPa to 92.6 MPa, see Fig. 6a and Table 2). With the reduced ability to withstand the opening stresses along its surface, the ply fails and delamination occurs according to the experimental results.

The matrix failure index was around 0.91 in Ply 16 (90°). One reason for the increased value is the decrease of the curvature approaching the outside of the radius which causes a stress

concentration. The other is the reduced in-situ strength of Ply 16, as it is an outer ply compared to Plies 1-15 which are embedded plies (Fig. 6a).

The highest value of the failure index in the filler was 0.56, located in the middle of its surface. Similarly to the plies, the vertical loading applied on the joint tries to straighten the curvature of the filler, generating high transverse tensile stresses on the surface, whereas shear stresses remained insignificantly low across the noodle. This phenomenon is represented by the vector of the maximum principal stress next to the highlighted element in Fig. 9a. The model cannot predict failure propagation, and thus the actual failure of the filler (last failure event) cannot be inspected. However, the principal stress vector rotated by 90° (Fig. 9a) can indicate the direction of the expected crack initiation, which is in accordance with the experimental results as a through-the-thickness crack initiated vertically before propagating along the ply interfaces (vertical crack in bottom left photo of Fig. 8).

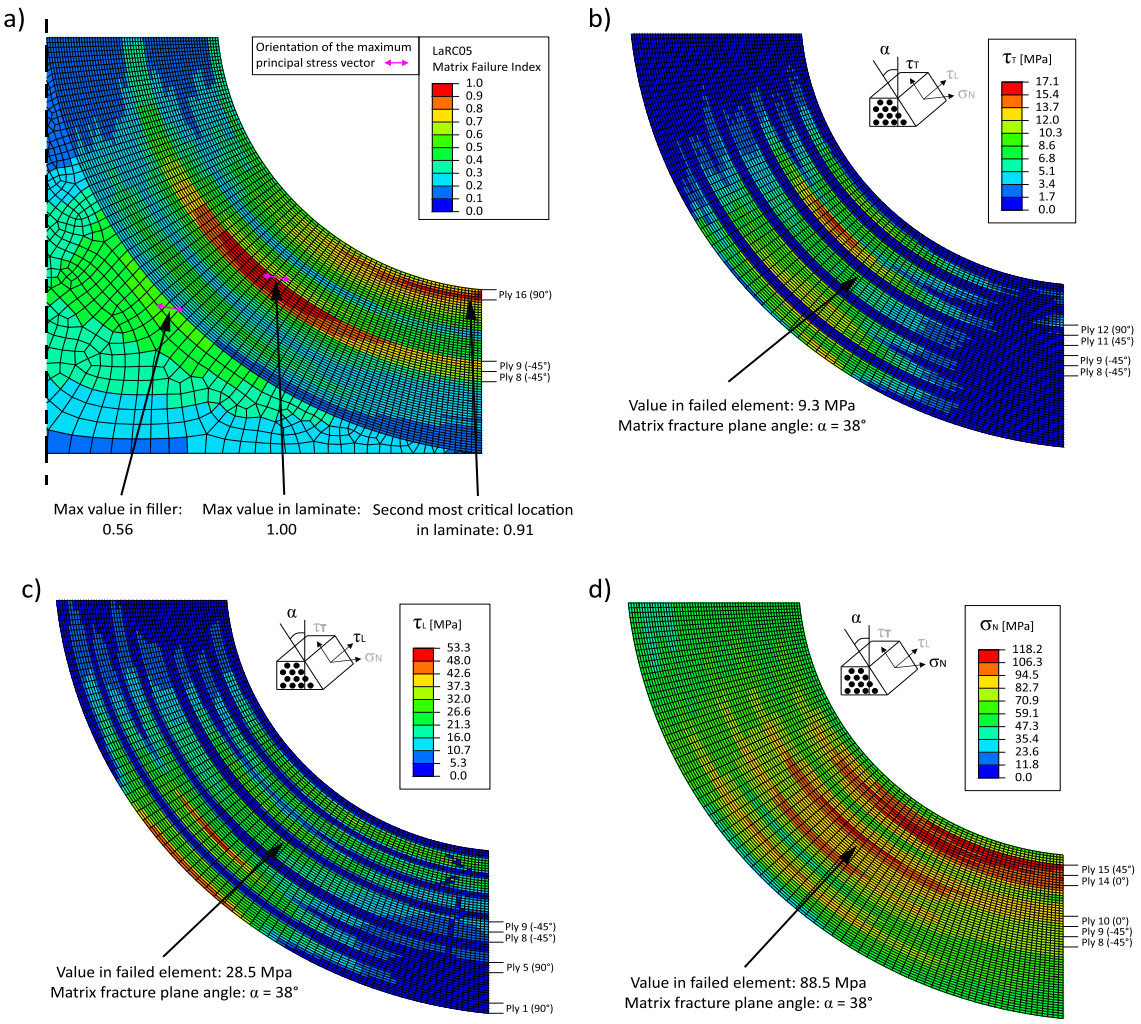

Fig. 9. a) LaRC05 matrix failure index at 4229 N applied load. Components of the matrix fracture plane: b) transverse shear component, c) longitudinal shear component, d) normal component

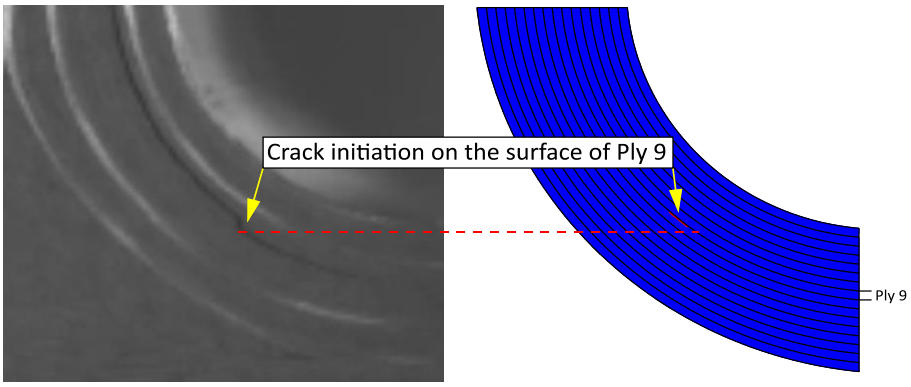

Fig. 10. Comparison of the experimental and numerical results. The crack initiates on the surface of Ply 9 at 4366 N average load in the specimen (left) and at 4229 N in the FEA model (right). The failed elements are highlighted with red

At the same load, the fibre tensile failure index is shown in Fig. 11. Being the outer ply with the smallest curvature and highest stiffness due to its 90° orientation, Ply 16 takes up the highest tensile load in the joint contributing to a 0.53 failure index value. Similarly, the 90° Ply 12 develops a failure index of 0.27 while the other the plies remain around or below 0.1. This matches the experimental results, as none of the plies failed due to fibre failure.

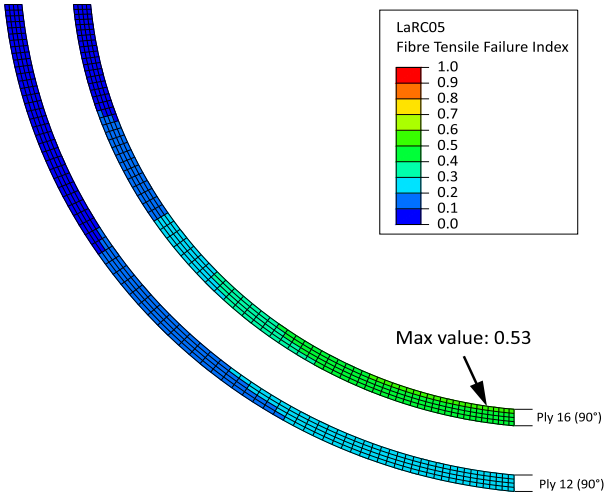

Fig. 11. LaRC05 fibre tensile failure index at 4229 N applied load

At the failure initiation load defined by the LaRC05 matrix failure criterion, none of the cohesive surfaces predicted failure (Fig. 12). Between Plies 9 and 10 (-45°/0° interface), where damage initiated according to experiments and LaRC05, the value of the quadratic nominal stress criterion was 0.72. The highest value across the radius was next to this interface between Plies 10 and 11 (0°/45°). One of the lowest values (0.43) was in the -45°/-45° stack in the midplane. This stack behaves as a single ply with double thickness, and delamination initiation is not expected to occur within it. The other lowest value (0.43) was on the boundary of the filler and the first ply (0°/90° interface). The reasons for the high strength of this interface are: 1) the low transverse stiffness and high effective ply thickness of the filler, which alleviate the delaminating stresses; 2) contrary to the laminate in the radius, the in-plane shear stresses in the filler were insignificantly low; and 3) this interface has the largest curvature and therefore the opening effect is the smallest here.

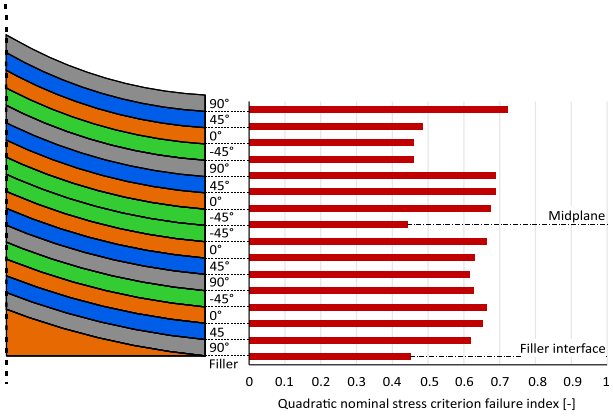

Fig. 12. Failure initiation values predicted by the cohesive zone via quadratic nominal stress criterion. Values are the maximum values across the interface in the radius and their location is in accordance with the critical locations of LaRC05 failure index shown in Fig. 9a.

4.4 Comparative studies

4.4.1 Effect of thermal expansion

The effect of thermal expansion and subsequent thermal stresses in the filler and radius before the application of the mechanical load can be seen in Fig. 13. The filler contains 0° fibres, thus it undergoes shrinking in the transverse direction when subjected to a decrease in temperature. The highest tensile stresses are 34 MPa and are located halfway between the middle and the edges of the noodle. The adjacent ply, having 90° orientation, not only has higher stiffness along the curvature but it also tries to expand due to its negative coefficient of thermal expansion. This mismatch in stiffness and thermal behaviour tries to open up the filler as shown by the orientation of the maximum principal stress vectors in Fig. 13a.

The behaviour of the plies in the laminate depended on their orientation and location in the stacking sequence. The first three 90° plies (Plies 1, 5, 12) underwent compression with the lowest compressive stress reaching the value of -272 MPa in Ply 1. This has great importance as this ply is subjected to further compressive stresses due to the bending of the corner geometry, however, failure did not occur as a result of compression in this particular T-joint configuration. The other plies were dominated by tensile thermal stresses. The maximum value in the 45° and -45° plies was 47 MPa and in the 0° plies it reached 42 MPa (Fig. 13b). The latter value occurred in the outer ply, thus it corresponds to 46% of its transverse tensile strength (92.3 MPa).

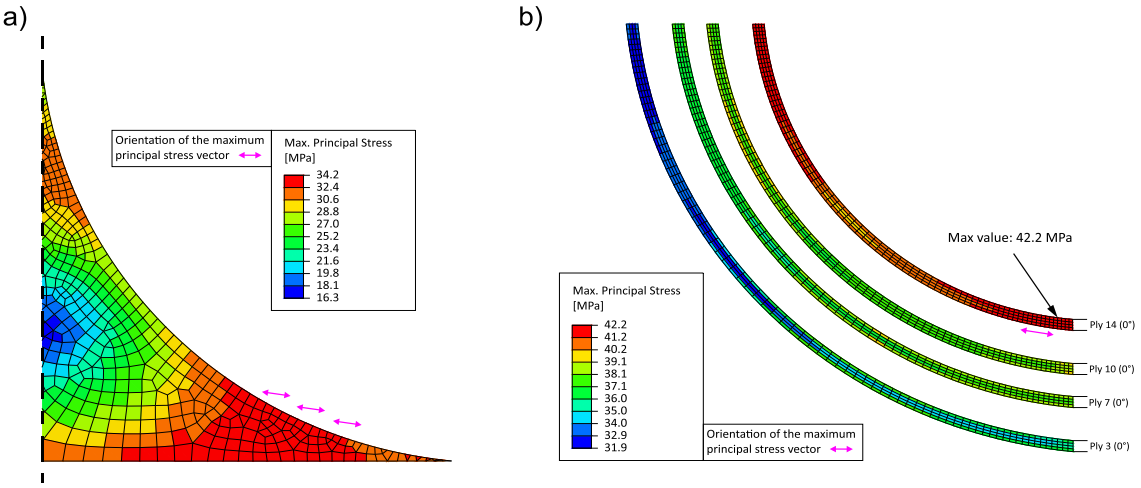

Fig. 13. Maximum principal thermal stresses before the application of mechanical load a) In the filler b) In 0° plies

Without thermal simulation the model predicted failure at 5147 N based on the cohesive model in the interface between Plies 15 and 16 (45°/90°), which is 18% higher than the experimental failure load. At the same load, the LaRC05 matrix failure index only reached the value of 0.88 in the same location where the model with thermal simulation predicted failure.

4.4.2 Effect of in-situ strengths

In-situ properties greatly increase the ply strengths and therefore have a significant impact on the failure behaviour of the joint. The default model (referred to as “S1”) introduced above was compared to two other variants: one that used UD strength in the laminate and the filler (referred to as “S2”) and one that used UD strength in the filler, but in-situ strength in the laminate(referred to as “S3”).

In the case where only UD strength was utilised (S2), the failure initiated at 2008 N according to LaRC05 matrix failure criterion, which is 54% lower than the experimentally observed value. At this load, where the default model accurately predicted failure along with the experimental results, the value of the index was 0.62 in the -45°/-45° interface (Plies 8-9). Instead, the failure

index reached 1 in Ply 15 (45°) (Fig. 14). This ply was critical in the default simulation too, but in this case, the failure sequence switched. The reason for this is the relative difference in increase due to the application of in-situ strengths. The transverse tensile strength of the stack formed by Plies 8 and 9 increased from 74.2 to 92.6 (embedded ply with double CPT), whereas the strength of Ply 15 increased to 131.0 MPa (embedded ply with single CPT). At this load, the failure index in the filler was 0.52, which is 247% larger than the 0.21 value in the default model.

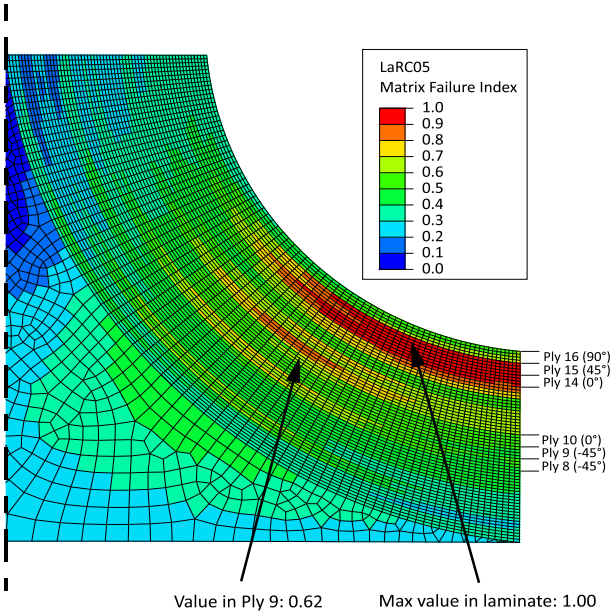

Fig. 14. LaRC05 matrix failure index around the filler when in-situ strengths are not utilised in the model (applied load = 2008 N)

In the third case, the in-situ strengths were utilised in the laminate but not in the filler (S3). In this case, the first event of failure occurred in the filler at 3386 N, whereas the value of LaRC05 matrix failure index was only 0.82 in the laminate, located in Ply 15. This refers to a 22% knock down compared to the experimental failure load.

The comparison of the three models are shown in Table 4. It can be seen that the conventional approach of using UD strength across the model (S2) significantly underpredicts the strength of

the joint and misses the failure location. The accuracy increases when in-situ strengths are utilised in the laminate (S3), but the failure location is still incorrect and the failure load prediction is off by 22%. To accurately simulate the initial failure load and failure location, it is necessary to use in-situ strength of the filler based on the filler effective ply thickness, as the filler behaves as a thick ply in the structure.

Table 4. Comparison of the models with different cases of UD and in-situ strength utilisation. The maximum failure index refers to the value of the LaRC05 matrix failure index

		Case		
	Experiment	**S1**	**S2**	**S3**
Strength used in the laminate	-	In-situ	UD	In-situ
Strength used in the filler	-	In-situ	UD	UD
Initial failure load [N]	4366	4229	2008	3386
Difference [%]	-	-3.1%	-54%	-22%
Initial failure location	Plies 8-9	Plies 8-9	Ply 15	Filler
Max. failure index in the laminate at 2008 N load	-	0.59	1.00	0.59
Max. failure index in the filler at 2008 N load	-	0.21	0.52	0.52
Max. failure index in the laminate at 3386 N load	-	0.89	>1	0.89
Max. failure index in the filler at 3386 N load	-	0.40	>1	1.00
Max. failure index in the laminate at 4429 N load	-	1.00	>1	>1
Max. failure index in the filler at 4429 N load	-	0.56	>1	>1

4.4.3 Effect of mesh refinement

As it can be seen in Fig. 4, increasing the number of elements across ply thickness from one makes a significant difference in predicted level of stress. In this study, the failure prediction of models with different number of elements per ply are compared.

With one element, the LaRC05 matrix failure index reached 1 near the end of curvature in Ply 16 at 3793 N (Fig. 15). This is not only a 10% lower failure load than predicted with 4 elements per ply thickness (and 13% lower compared to the experimental value), but the location also moved from Ply 9 to Ply 16. The failure index in Ply 9 at the same load is 0.83.

Modelling the plies with two elements also predicts failure in the outer Ply 16, and the crack location only becomes accurate (Ply 9) after increasing the density to three elements. Two and three elements underpredict the strength by 9% and 6%, respectively, compared to the

experiment. The difference converges below 5% by increasing the element number to four, and stays below this value when increasing it further to five and six elements.

Therefore, in this application it is required to model the plies with at least three elements per ply to capture the failure location and with at least four elements per ply to achieve a converged value.

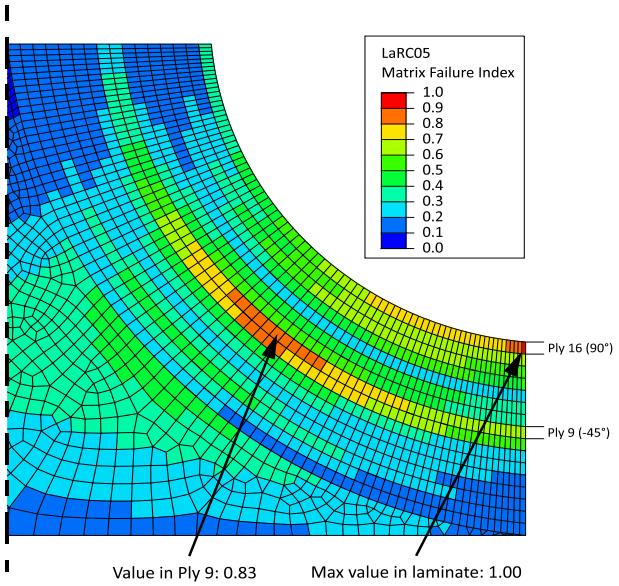

Fig. 15. LaRC05 matrix failure index around the filler when plies are modelled with one element across ply thickness (applied load = 3793 N)

5. Conclusions

A high-fidelity FEA model is introduced and experimentally validated to simulate the initial failure of a T-joint subjected to tensile loading. The simulation predicts matrix failure according to LaRC05 failure criterion in the radius at 4229 N, which matches the average of the test results with 3% accuracy and predicts the same failure initiation location.

To ensure the accuracy of the simulation, a highly controlled manufacture and testing procedure is utilised and the specimen geometry, including the shape of the filler and the variable ply thickness across the joint, is adjusted in the model. Moreover, in-situ strengths are

implemented and a new phenomenon, the effective ply thickness of the filler is introduced to account for its in-situ strength properties.

It is demonstrated that the currently used simulation approach of using mechanical properties measured with unidirectional coupons might not be sufficient for the analysis of more complex structures on higher levels of the test-pyramid. Instead, a better understanding of the interaction between the plies and surrounding components (e.g. filler) in the laminate is required by the usage of in-situ properties and physically based failure criterion. Furthermore, the moisture content, thermal stress state and manufactured geometry (such as filler shape and ply thickness) of the specimens need to be matched in the simulation. Finally, contrary to the common approach in the literature, the number of elements across ply thickness must be higher than one, otherwise the peak values of stress cannot be captured and the simulation can incorrectly predict the strength of the structure.

Because of the unstable failure behaviour of out-of-plane joints, the design of these structures is usually driven by the initial failure strength of the component, which can be accurately captured by the numerical model presented here and therefore can be used in the design process. Due to its linear elastic assumption and therefore low computational requirements, the proposed framework might be useful for optimisation studies and development of design rules and stacking sequence guidelines for similar T-joints. However, the validity of the model for the prediction of other modes of failure is untested; future work should focus on such validation.

Acknowledgement

Zsombor Sápi would like to thank GKN Aerospace for sponsoring the project. Richard Butler holds a Royal Academy of Engineering – GKN Aerospace Research Chair.

References

[1] Teixeira de Freitas S, Sinke J. Failure analysis of adhesively-bonded skin-to-stiffener joints: Metal-metal vs. composite-metal. Engineering Failure Analysis 2015;56:2–13. doi:10.1016/j.engfailanal.2015.05.023.

[2] Teixeira de Freitas S, Sinke J. Failure analysis of adhesively-bonded metal-skin-to-composite-stiffener: Effect of temperature and cyclic loading. Composite Structures 2017;166:27–37. doi:10.1016/j.compstruct.2017.01.027.

[3] Sápi Z, Butler R, Rhead A. Filler materials in composite out-of-plane joints – A review. Composite Structures 2019;207:787–800. doi:10.1016/j.compstruct.2018.09.102.

[4] Hélénon F, Wisnom MR, Hallett SR, Trask RS. Numerical investigation into failure of laminated composite T-piece specimens under tensile loading. Composites Part A: Applied Science and Manufacturing 2012;43:1017–27. doi:10.1016/j.compositesa.2012.02.010.

[5] Chen J, Fox D. Numerical investigation into multi-delamination failure of composite T-piece specimens under mixed mode loading using a modified cohesive model. Composite Structures 2012;94:2010–6. doi:10.1016/j.compstruct.2011.12.030.

[6] Bai JB, Shenoi RA, Yun XY, Xiong JJ. Progressive damage modelling of hybrid RTM-made composite pi-joint under four-point flexure using mixed failure criteria. Composite Structures 2017;159:327–34. doi:10.1016/j.compstruct.2016.09.083.

[7] Zhao L, Qin T, Chen Y, Zhang J. Three-dimensional progressive damage models for cohesively bonded composite pi joint. Journal of Composite Materials 2014;48:707–21. doi:10.1177/0021998313477169.

[8] Zhao L, Qin T, Zhang J, Shenoi RA. Modified maximum stress failure criterion for composite π joints. Journal of Composite Materials 2012;47:2995–3008.

doi:10.1177/0021998312460713.

[9] Cui H. Delamination and debonding failure of laminated composite T-joints. PhD thesis. Delft University of Technology, 2014. doi:10.4233/uuid:fcf6a51a-1abd-4751-8ae5-338dbb23bce2.

[10] Trask RS, Hallett SR, Helenon FMM, Wisnom MR. Influence of process induced defects on the failure of composite T-joint specimens. Composites Part A: Applied Science and Manufacturing 2012;43:748–57. doi:10.1016/j.compositesa.2011.12.021.

[11] Matveev MY, Belnoue JP-H, Nixon-Pearson OJ, Ivanov DS, Long AC, Hallett SR, et al. A numerical study of variability in the manufacturing process of thick composite parts. Composite Structures 2018;208:23–32. doi:10.1016/j.compstruct.2018.09.092.

[12] Hexcel Composites. HexPly 8552 product data sheet, publication FTA 072e; 2013.

[13] Hélénon F, Wisnom MR, Hallett SR, Trask RS. Investigation into failure of laminated composite T-piece specimens under bending loading. Composites Part A: Applied Science and Manufacturing 2013;54:182–9. doi:10.1016/j.compositesa.2013.07.015.

[14] Pinho ST, Darvizeh R, Robinson P, Schuecker C, Camanho P. Material and structural response of polymer-matrix fibre-reinforced composites. Journal of Composite Materials 2012;46:2313–41. doi:10.1177/0021998312454478.

[15] Davila CG, Camanho PP, Rose CA. Failure criteria for FRP laminates. Journal of Composite Materials 2005;39:323–45. doi:10.1177/0021998305046452.

[16] Camanho PP, Dávila CG, Pinho ST, Iannucci L, Robinson P. Prediction of in situ strengths and matrix cracking in composites under transverse tension and in-plane shear. Composites Part A: Applied Science and Manufacturing 2006;37:165–76. doi:10.1016/j.compositesa.2005.04.023.

[17] Catalanotti G. Prediction of in situ strengths in composites: some considerations. Composite Structures 2018;207:889–93. doi:10.1016/j.compstruct.2018.09.075.

[18] Camanho PP. Progressive failure analysis of advanced composites. University of Porto report FR-FA8655-06-1-3072. 2008.

[19] Marlett K. Hexcel 8552 AS4 unidirectional prepreg at 190 gsm & 35% RC qualification material property data report. NCAMP test report CAM-RP-2010-002 Rev A. 2011.

[20] Pinho ST, Dávila CG, Camanho PP, Iannucci L, Robinson P. Failure models and criteria for FRP under in-plane or three-dimensional stress states including shear non-linearity. NASA report TM-2005-213530. 2005.

[21] Turon A, Dávila CG, Camanho PP, Costa J. An engineering solution for mesh size effects in the simulation of delamination using cohesive zone models. Engineering Fracture Mechanics 2007;74:1665–82. doi:10.1016/j.engfracmech.2006.08.025.

[22] Harper PW, Hallett SR. Cohesive zone length in numerical simulations of composite delamination. Engineering Fracture Mechanics 2008;75:4774–92. doi:10.1016/j.engfracmech.2008.06.004.

[23] Camanho PP, Dávila CG, de Moura MF. Numerical simulation of mixed-mode progressive delamination in composite materials. Journal of Composite Materials 2003;37:1415–38. doi:10.1177/0021998303034505.

[24] Falcó O, Ávila RL, Tijs B, Lopes CS. Modelling and simulation methodology for unidirectional composite laminates in a Virtual Test Lab framework. Composite Structures 2018;190:137–59. doi:10.1016/j.compstruct.2018.02.016.

[25] Pinho S, Vyas G, Robinson P. Response and damage propagation of polymer-matrix fibre-reinforced composites: Predictions for WWFE-III Part A. Journal of Composite

Materials 2013;47:2595–612. doi:10.1177/0021998313476972.

[26] Li M, Wang X, Xie F, Zhang Z. Influence of fillers in stiffener core and structural parameters on compaction of T-stiffened skins in autoclave process. Polymers & Polymer Composites 2009;17:273–80.